Extracting reliable P-wave reflections from teleseismic P wave coda autocorrelation

Jinju Zhou[1] and Wei Zhang[2]

[1]China University of Mining and Technology
[2]Southern University of Science and Technology

November 24, 2022

Abstract

Recently, many studies have demonstrated the use of teleseismic P wave coda autocorrelation for imaging lithosphere structures. However, the reliability of the extracted reflections remains uncertain and a means of evaluation is lacking. In this paper, we propose a velocity analysis method that conveniently solves this problem in place of a synthetic experiment. This method considers the average velocity used for the horizontal slowness correction as an unknown quantity, and then uses the continuously varying average velocity for the horizontal slowness correction. Finally, this method obtains a stacked result that varies with the average velocity and the vertical two-way travel time to produce a va-t0 diagram. This method is similar to the velocity analysis method used in exploration geophysics. In this diagram, reliable reflections correspond to focused energy clusters, while noise lacks this feature. Therefore, this method helps determine which reflections are reliable, while also finding the appropriate parameters for data processing. Synthetic data tests were performed to demonstrate the validity of this method, as well as a test of field data for station BOSA, which illustrates the successful application of the method in the case of a sharp and flat Moho discontinuity. Finally, we applied the method to the NCISP-6 dense array, and observed obvious energy clusters representing reflections from the Moho discontinuity in the results of most stations. The depth and shape of the Moho discontinuity determined by this test is consistent with receiver function results, which verifies the robustness of this method in relatively complex applications.

Extracting reliable P-wave reflections from teleseismic P wave coda autocorrelation

Jinju Zhou[1,2], Wei Zhang[1]

[1]Southern University of Science and Technology, Department of Earth and Space Sciences
[2]China University of Mining and Technology, School of Resources and Geosciences

Key Points:

- Extracting reflections from teleseismic P wave coda autocorrelation is well established, but there is a need to evaluate their reliability.
- We propose a velocity analysis method that can conveniently solve this problem in place of a synthetic experiment.
- Synthetic data tests and field data examples demonstrate the validity of this method.

Corresponding author: Wei Zhang, zhangwei@sustech.edu.cn

Abstract
Recently, many studies have demonstrated the use of teleseismic P wave coda autocorrelation for imaging lithosphere structures. However, the reliability of the extracted reflections remains uncertain and a means of evaluation is lacking. In this paper, we propose a velocity analysis method that conveniently solves this problem in place of a synthetic experiment. This method considers the average velocity used for the horizontal slowness correction as an unknown quantity, and then uses the continuously varying average velocity for the horizontal slowness correction. Finally, this method obtains a stacked result that varies with the average velocity and the vertical two-way travel time to produce a v_a−t_0 diagram. This method is similar to the velocity analysis method used in exploration geophysics. In this diagram, reliable reflections correspond to focused energy clusters, while noise lacks this feature. Therefore, this method helps determine which reflections are reliable, while also finding the appropriate parameters for data processing. Synthetic data tests were performed to demonstrate the validity of this method, as well as a test of field data for station BOSA, which illustrates the successful application of the method in the case of a sharp and flat Moho discontinuity. Finally, we applied the method to the NCISP-6 dense array, and observed obvious energy clusters representing reflections from the Moho discontinuity in the results of most stations. The depth and shape of the Moho discontinuity determined by this test is consistent with receiver function results, which verifies the robustness of this method in relatively complex applications.

1 Introduction

Existing methods for extracting P-wave reflections from the coda of the teleseismic first-P phase (or global phase PKIKP) are based on the hypothesis of Claerbout (1968). The P-wave reflections of horizontally stratified acoustic media can be retrieved from autocorrelation of plane-wave transmission. Ruigrok and Wapenaar (2012) extended the hypothesis to global-scale seismology and referred to the method as global-phase seismic interferometry (abbreviated as GloPSI). Like PKIKP the global phase (with an epicentral distance greater than 120 degrees) propagates through the upper mantle in a nearly planar orientation before arriving at seismic stations. The coda wave of the PKIKP phase contains reverberations in the lithosphere and the vertical component is a good approximation of the P-wave transmission response. So GloPSI is consistent with the original setting of Claerbout (1968). Using this method, they extracted P-wave reflections from crustal structures below the Himalayas and Tibet and demonstrated that GloPSI can be used to image crustal structures. However, their results contained discontinuous reflections of the Moho and included many reflections of uncertain origin. These features rendered the interpretation of the results difficult and unreliable. Nishitsuji et al. (2016) also employed this method to image the aseismic zones of the Nazca slab. They found an attenuated zone at a depth deeper than the Moho, which is consistent with the presence of an aseismic dipping subducting slab. This demonstrated the potential of GloPSI to image structures below the Moho. However, the authors stated that their interpretation was not unambiguous because many reflections in the image were difficult to interpret.

In practice, the events used by GloPSI (epicentral distances greater than 120 degree) are usually few. For example, the number of phases utilized in the study of the Tibet subarray and the Himalaya subarray are 17 and 34, respectively (Ruigrok & Wapenaar, 2012). Since the individual autocorrelograms contain noise due to the source and raypath, a sufficient number of autocorrelograms must be available to efficiently suppress the noise by stacking. This may be the cause of the artifacts in their results. To utilize as many events as possible, Sun and Kennett (2016) proposed a method, seismic daylight imaging, which used events with epicentral distances between 30 and 90 degrees. They then used this method to obtain an image of the mid-lithosphere discontinuity beneath the western and central parts of the North China Craton (NCC) (Sun & Kennett, 2017). They attempted to reveal fine-scale structures in the lithosphere by using a broad high-frequency band (0.5-4 Hz); however, clear reflections of the Moho or the mid-lithosphere discontinuity cannot be readily identified from their results. This ambiguity may adversely affect the reliability of such interpretations, despite the principles presented in another paper (Sun et al., 2018). In addition, the use of Bayesian inversion in P wave coda autocorrelation for crustal imaging (Tork Qashqai et al., 2019), may produce stable inversions from clear reflections.

Therefore, extracting clear reflections and suppressing noise are the two main difficulties of the P wave coda autocorrelation method. By adding spectral whitening before autocorrelation and using a phase-weighted stack method, Phạm and Tkali (2017) successfully extracted a clear reflection of the Moho below the bedrock station BOSA from the teleseismic P wave coda. They further applied this method to investigate properties of the Antarctic ice sheet (Phạm & Tkali, 2018). Using a similar procedure, Plescia et al. (2020) reported a successful application of the method for imaging upper crustal and basin structures. This demonstrated the ability of the autocorrelation method to recover clear reflections and its potential to image shallow structures. In this study, we propose a method for solving a related issue: namely, how to evaluate the reliability of the reflections extracted by autocorrelation. This issue is very important for the extraction of reflections and distinguishing between reflections and artifacts in interpretation.

Our proposed method is based on the observation that there are differences in the time delays of reflections extracted by autocorrelation of the coda wave of events with different ray parameters. This time difference can only be cancelled by the correct P-wave velocity, assuming that the ray parameters of the events are known. These corrected autocorrelograms are then stacked and we use the continuously varying P-wave velocity to correct the autocorrelograms. Finally, we obtain a stacked result that varies with the P-wave velocity and the vertical two-way travel time, that is, a v_a−t_0 diagram. In this diagram, reliable reflections correspond to focused energy clusters, whereas noise is not associated with this feature. In the next section, we first derive the arrival time formula of the reflection extracted from the P wave coda autocorrelation and then present our proposed velocity analysis method based on this formula. We use a synthetic data test to show the potential of this method for extracting reliable reflections. In section 3, we apply this method to field data from station BOSA to test the validity of this method in the case of a sharp and flat Moho discontinuity. We then apply this method to the field data of a dense array NCISP-6 in section 4 to test the robustness of this method in relatively complex situations. Finally, we present our conclusions and prospects for future study.

2 Methods

2.1 Teleseismic P-coda autocorrelation

When seismic waves from distant earthquakes arrive at seismic stations, they propagate nearly vertically in the upper mantle. Their coda waves contain reverberations in the lithosphere, so the reflections of crust and upper mantle structures can be extracted by autocorrelating the coda wave. We use the relationship demonstrated by Ruigrok and Wapenaar (2012) here,

$$v_z(-t, x_i) * v_z(t, x_i) = -R(-t, x_i) + \delta(t) - R(t, x_i), \tag{1}$$

where $v_z(t, x_i)$ is the vertical-component record, $R(t, x_i)$ is the retrieved P-wave reflection response, $\delta(t)$ is a delta pulse, $*$ denotes convolution, and x_i represents the i^{th} station. Equation 1 shows the relationship of seismic records and retrieved P-wave reflection responses for one teleseismic event. The autocorrelation of seismic records includes

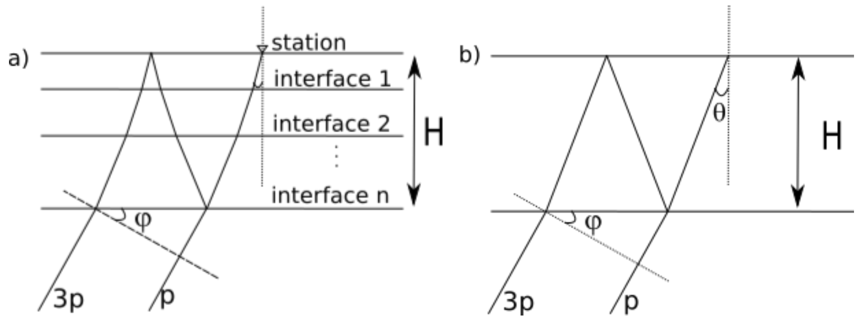

Figure 1. Schematic representation of a plane wave approaching a receiver and its first-order reverberations. The left panel shows the case for crust that contains many layers, and the right panel shows an approximation of crust that is regarded as a single layer.

three parts. The causal part of the autocorrelation after muting the delta pulse and inverting the polarity is the retrieved P-wave reflection response.

In practice, stacking as many autocorrelation results as possible is needed to enhance the effective reflection response and to suppress irregular noise. Ruigrok and Wapenaar (2012) directly stacked the autocorrelation results after spectral balancing. For GloPSI, this is reasonable because the incidence of the global seismic phase is nearly perpendicular below the station. In this case, the time difference caused by the horizontal slowness of different phases is relatively small. The seismic phase from teleseismic events (epicentral distances between 30 and 95 degrees) cannot be regarded as having a near-vertical incidence and the time difference caused by the horizontal slowness of different phases cannot be neglected. Sun and Kennett (2016) suggested that a moveout correction should be applied to the autocorrelograms of each event before stacking. They give a moveout correction function in the $\tau - p$ domain,

$$\tau_0 \approx \tau/(1 - \frac{1}{2}v_0^2p^2), \tag{2}$$

where τ_0 is the vertical reflection time, τ is the real arrival time of the retrieved reflection response, and v_0 is the average velocity above an interface. The correction function was deduced from the relationship between the vertical reflection time and the real arrival time. After the moveout correction, the signal-to-noise ratio of the superimposed result clearly improves.

2.2 Arrival time formula

When a plane wave is incident on an inhomogeneous multi-layer medium (left panel in Figure 1), the arrival time of the reflection for interface n retrieved from teleseismic P-coda autocorrelation can be determined as,

$$t = t_{3p} - t_p = 2\sum_{i=1}^{n} \frac{h_i}{cos\theta_i v_i} - \frac{2\sum_{i=1}^{n} h_i tan\theta_i sin\psi}{V_m} \tag{3}$$

where h_i, v_i, and θ_i are the thickness, P-wave velocity, and incident angle in each layer, respectively. V_m and ψ are respectively the P-wave velocity and incident angle below the Moho.

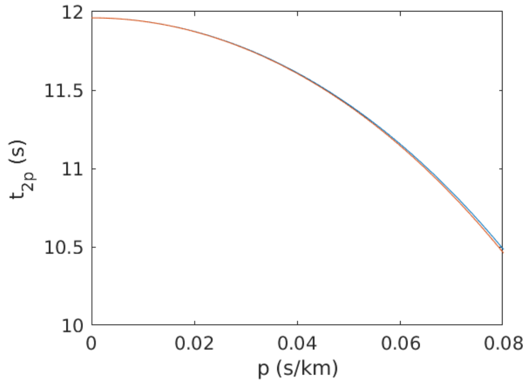

Figure 2. Comparison of arrival times calculated from the average velocity (blue line) and the real layer velocity (red line).

Taking the horizontal slowness ($p = \frac{sin\theta_i}{v_i} = \frac{sin\psi}{V_m}$) of the incident plane wave, Equation 3 can be rewritten as

$$t = 2\sum_{i=1}^{n} \frac{h_i}{v_i\sqrt{1-p^2v_i^2}} - 2p^2\sum_{i=1}^{n} \frac{h_iv_i}{\sqrt{1-p^2v_i^2}}. \tag{4}$$

Equation 4 contains the thickness and velocity of each layer, which is difficult to use in practice.

Here we introduce an average velocity V_a above the target interface. It is defined as,

$$V_a = \frac{\sum_{i=1}^{n} h_i}{\sum_{i=1}^{n} \frac{h_i}{v_i}} \tag{5}$$

In this case (right panel in Figure 1), the arrival time of the reflection retrieved from P wave coda autocorrelation can be determined as,

$$t = t_{3p} - t_p = \frac{2H}{V_a cos\theta} - \frac{2Htan\theta sin\psi}{V_m}. \tag{6}$$

where H is the depth of target interface n. Equation 6 is then reduced to

$$t = \frac{2H}{V_a}cos\theta = t_0\sqrt{1-p^2V_a^2}. \tag{7}$$

where t_0 is the vertical two-way arrival time of the reflection at target interface n.

We can then test the validity of using the average velocity as an approximation of the layered velocity. For crust containing three layers with thicknesses of 5, 23, and 8 km, the P-wave velocity of each layer is 4.671, 6.228, and 6.574 km/s, respectively. The average velocity can be calculated as 6.0197 km/s using Equation 5. For an incident plane wave with horizontal slowness ranging from 0 to 0.08 s/km, a comparison of arrival times calculated from the average velocity and the real layer velocity is shown in Figure 2. It is apparent that the difference in arrival times between these two methods is small; therefore, the approximation is acceptable.

2.3 Moveout correction and stacking

Using Equation 7, we proposed a stacking formula (Equation 8) that directly includes the moveout correction:

$$R_0(t_0, x_i) = \frac{1}{N}\sum_{e_i=1}^{N} R(t_0(\sqrt{1-p^2v_{a,t_0}^2}), x_i, e_i) \tag{8}$$

where, R_0 is a linear-stack zero-offset reflection response, R is the reflection response retrieved using Equation 1, x_i represents th i^{th} station, e_i represents the i^{th} event, and v_{a,t_0} represents the average velocity at t_0 time, which is converted from the reference velocity model. For synthetic data, the reference velocity model is the true velocity model. For field data, the reference velocity model can be the known P-wave velocity model (2-D or simply 1-D, as in IASP91 or PREM) in the research area or scanned as described in section 2.4.

The retrieved reflections are directly linearly stacked using Equation 8. We also give a formula (Equation 9) for correcting the retrieved reflections to use with other stacking methods (like the phase-whited stacking method) or for comparing reflections before and after the horizontal slowness correction:

$$R_s(t_0, x_i, e_i) = R(t_0(\sqrt{1-p^2v_{a,t_0}^2}), x_i, e_i) \tag{9}$$

where, R_s is the corrected reflection. The corrected reflections can then be linearly stacked or stacked using the phase-whited stacking (PWS) method (Schimmel & Paulssen, 1997). Here, we follow the equations in Phạm and Tkali (2017). The analytical signals of the corrected reflections are defined as:

$$\mathbf{R}_s(t_0, x_i, e_i) = R_s(t_0, x_i, e_i) + iH(t_0, x_i, e_i) = A(t_0, x_i, e_i)e^{i\Phi(t_0, x_i, e_i)} \tag{10}$$

where $H(t_0, x_i, e_i)$ is the Hilbert transform of the original trace $R_s(t_0, x_i, e_i)$, and $A(t_0, x_i, e_i)$, $\Phi(t_0, x_i, e_i)$ are the amplitude and phase components. Then the linear stack is weighted using the amplitude of the analytical phase average:

$$R_{0,PWS}(t_0, x_i) = \frac{1}{N}\sum_{e_i=1}^{N} R_s(t_0, x_i, e_i)\left|\frac{1}{N}\sum_{e_i=1}^{N} e^{i\Phi_n(t_0, x_i, e_i)}\right|^{\eta} \tag{11}$$

where $\eta >= 0$ is the PWS order and $R_{0,PWS}(t_0, x_i)$ is the phase-weighted stack. The order of PWS, η, controls the contribution of the overall coherency measure in the final stack. In our study, we found that a first order PWS ($\eta = 1$) is sufficient to suppress noise.

2.4 Velocity analysis method

We have presented the details of the proposed stacking method above. However, the arrival time formula (Equation 7) has other potential applications in addition to the moveout correction. It contains the relationship between the real arrival time (t) of the retrieved reflection, the vertical reflection time (t_0), and the average P-wave velocity (V_a) above an interface. Then, if we regard V_a as an unknown quantity, we can express it as a continuously varying quantity. Here, we give the formula for velocity analysis based on Equation 7,

$$I_v(t_0, v_i, x_i) = \frac{1}{N}\sum_{e_i=1}^{N} R(t_0(\sqrt{1-p^2v_i^2}), x_i, e_i) \tag{12}$$

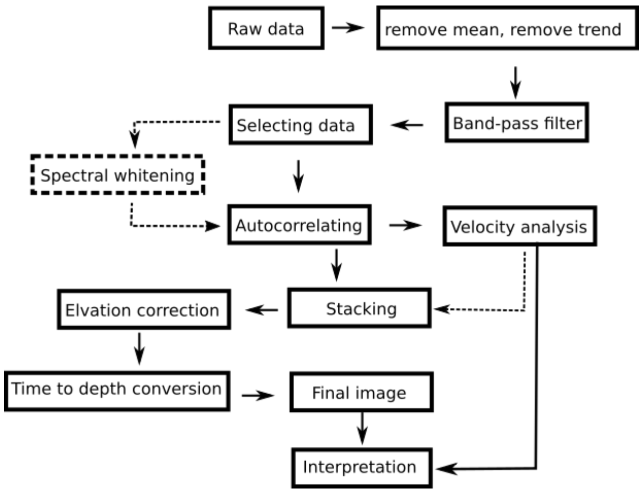

Figure 3. Illustration of the data processing workflow.

where, I_v is the linear-stack zero-offset reflection response for velocity analysis and v_i is the stacking velocity variable. For each stations, I_v is a $V_a - t_0$ map, which is similar to the velocity spectrum in exploration geophysics. In the $V_a - t_0$ map, there will be some energy groups. The maximum value of each energy group is the maximum amplitude to which the corresponding reflection response can be superimposed.

The PWS method also can be used in the velocity analysis step. In this case, Equation 12 is rewriten as

$$I_{v,PWS}(t_0, v_i, x_i) = \frac{1}{N} \sum_{iev=1}^{N} R_s(t_0, v_i, x_i, iev) \left| \frac{1}{N} \sum_{iev=1}^{N} e^{i\Phi_n(t_0, v_i, x_i, iev)} \right|^{\eta} \tag{13}$$

where $I_{v,PWS}$ is the phase-weighted stack for velocity analysis. Here, R_s has only one more v_i parameter than in Equation 9, which means that the retrieved reflections R are corrected with the variable velocity v_i instead of the reference velocity v_{a,t_0}. The complete data processing workflow is shown in Figure 3.

First, mean removal and trend removal are performed on the raw vertical seismic records in the data preprocessing step. Since the autocorrelation method is a single station method, the effect of the instrumental response removal is minor (Gorbatov et al., 2013), so removing the instrument response is optional in the data preprocessing step. Then, the preprocessed data is filtered to a suitable frequency range to facilitate the selection of ideal events. Ideal events are those with a clear P-wave onset and with no noticeable noise prior to the P-wave onset. Additionally, the absence of interference from other strong amplitude phases in the coda window is preferable. The selected events can be directly subjected to autocorrelation, or a spectral whitening step can be added before the autocorrelation. On the one hand, spectral whitening can improve the high-frequency content of a single event, and on the other hand, it can balance the spectrum difference between different events. This is helpful for improving the signal-to-noise ratio of stacking results. The causal part (positive time part) of the autocorrelation result is the extracted reflection response with a virtual source and geophone on the surface. The extracted reflection responses are then used in the velocity analysis step (using Equations 12 or 13). The $v_a - t_0$ velocity analysis map contains focused energy clusters, and the coordinates of the local maximum of each energy cluster indicates the average velocity (v_a) and vertical two-way travel time (t_0) above a certain interface. The depth of this

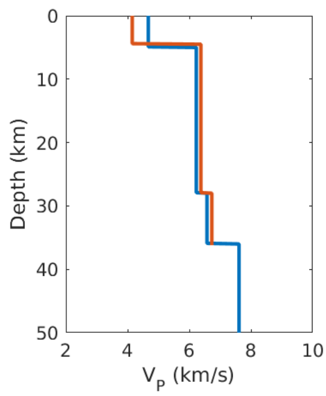

Figure 4. P-wave velocity of our 1-D model. The blue line represents the real velocity and the red line represents the velocity estimated from velocity analysis.

interface can be calculated from v_a and t_0. From the local maxima of multiple energy clusters, an average velocity curve can be determined in the subsequent superposition step. While this procedure is feasible for synthetic data testing, the complexity of field data may cause it to become unreliable at some stations. When a relatively good velocity model is known, the known velocity model can be used in the stacking step. The stacking step can be done using a linear stack including the horizontal slowness correction (Equation 8), or Equation 9 can first be used for the horizontal slowness correction, followed by the PWS method (Equation 11). The stacked reflection responses are then subjected to an elevation correction and a time-to-depth conversion to obtain the final image. Finally, the structure may be interpreted based on the image. Here, the velocity analysis results become very important, because they indicate which reflections are reliable and which are not.

2.5 Synthetic data test

A four-layer, one-dimensional model (blue line in Figure 4) was used to test the velocity analysis method and stacking formula. The V_P/V_S ratio is 1.73. To obtain the synthetic data, we use the *respknt* program which was written by Randall (1994) and is based on Kennett (1983). A total of 93 records were modeled. The horizontal slowness of the incident plane-wave used for synthetic data was randomly picked from the range 0.04-0.08. The records have been filtered using a 4-points Butterworth bandpass filter with corners at 0.1-2.0 Hz before autocorrelation. The 93 autocorrelograms are arranged according to the horizontal slowness from small to large in Figure 5 (left panel). In this figure, the Moho reflection is distributed along the blue curve (the arrival time curve is calculated by Equation 7 with $t_0 = 11.975s$ and $v_a = 6.05km/s$). If we assume that the horizontal slowness parameter is known, we can stack these autocorrelograms with continuously varying velocity parameters. Only the correct velocity can make these autocorrelograms stack to the maximum value. Finally, we obtain the stacked autocorrelogram with varying velocity (that is the V_a-t_0 diagram). This is the theoretical basis of velocity analysis. Since no noise is added to the synthetic data and the spectrum components of different events are the same, the PWS method and spectral whitening were not used in this test.

The velocity analysis result (calculated using Equation 12) is shown in the left panel of Figure 6. In order to suppress the influence of the source time function, the first 5s of records in the autocorrelograms were weakened by a Hanning window before velocity analysis. There are two distinct energy groups along the reference average velocity

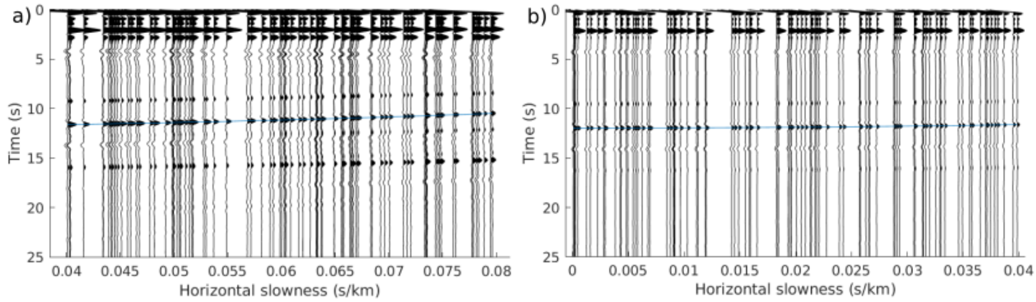

Figure 5. Sorted autocorrelograms with horizontal slowness arranged from small to large. Horizontal slowness in the left panel ranged from 0.04 to 0.08, while in the right panel it ranges from 0 to 0.04

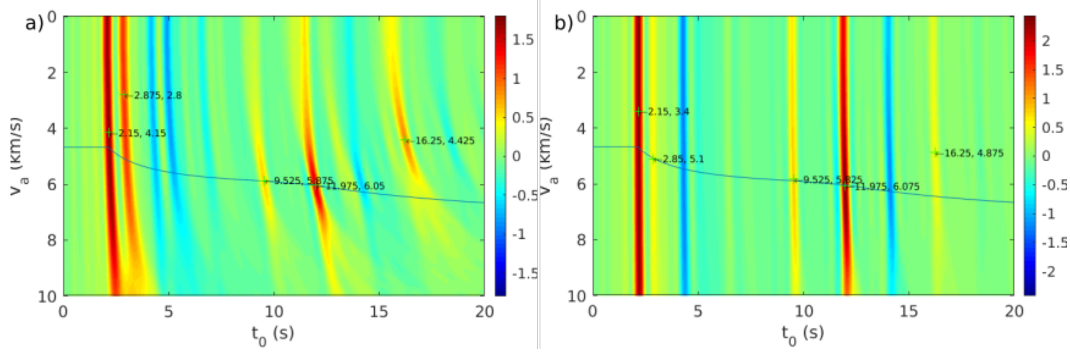

Figure 6. Velocity analysis results of two datasets (left: horizontal slowness [0.040.08], right: horizontal slowness [00.04]).

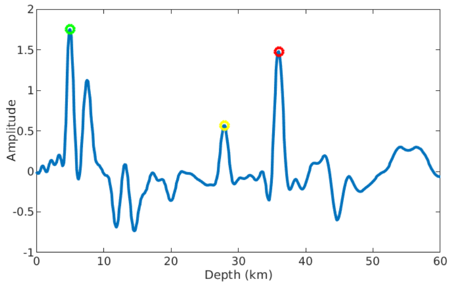

Figure 7. Stacked zero-offset reflections after conversion to the depth domain

curve (blue line) at about the 10-second and 12-second positions. The local maxima of the two energy groups are marked by the green crosses that intersect the blue line. Their coordinates indicate average velocities (5.875 km/s and 6.05 km/s) and vertical two-way travel times (9.525 s and 11.975 s) corresponding to the two interfaces. Compared with the reference average velocity (5.89 km/s and 6.04 km/s) at same time, the errors in the estimated average velocity are 0.25% and 0.17%. Furthermore, we can estimate the depths of these two interfaces to be 27.98 kilometers and 36.22 kilometers, respectively, based on the estimated average velocity and vertical two-way travel time. Compared with the real depth of the two interfaces (28 km and 36 km), the errors in the estimated depth are only 0.07% and 0.61%. Therefore, the average velocity distribution and subsurface structures may be reasonably estimated based on this velocity analysis method.

The energy group with a local maximum at (16.25 s, 4.425 km/s) may correspond to the PS reflection of the Moho, because it arrives later and has a low average velocity compared to the reference average velocity. The energy group with a local maximum at (2.15 s, 4.15 km/s) corresponds to the PP reflection of the first interface. The other group with a local maximum at (2.875 s, 2.8 km/s) may correspond to the PS reflection of the first interface. The estimated average velocity above the first interface (4.15 km/s) deviates significantly from the reference value, with an error about 12.4%. This is because the reflection in this frequency band is also affected by the source time function. If the frequency is increased, this method can also estimate the average velocity distribution and structures of the shallow subsurface.

Furthermore, we estimated the interval velocity distribution based on the estimated average velocity and vertical two-way travel time. The result is shown by the red line in Figure 4. Except for the first layer, the estimated interval velocity is in good agreement with the real interval velocity.

Next, the autocorrelograms are stacked using Equation 8 and converted from the time domain to the depth domain, referring to the theoretical P-wave average velocity. The result is shown in Figure 7. The two positive values at 28 km (yellow circle) and 36 km (red circle) correctly indicate the two interface positions. Even the position of the first interface (5 km, marked by the green circle) also can be identified.

In theory, for global phases (where the epicentral distance is greater than 120 degrees, that is, the horizontal slowness is less than 0.04), there is no need to perform a slowness correction before stacking. Here we also give the autocorrelograms (right panel in Figure 5) and velocity analysis results (right panel in Figure 6) for this case. The curvature of the Moho reflection is small in the autocorrelograms, showing that the Moho reflection can be superimposed without a slowness correction. The velocity analysis results also demonstrate this point. The Moho reflection energy cluster in the velocity analysis result is not as focused as that of the teleseismic phases (horizontal slowness between

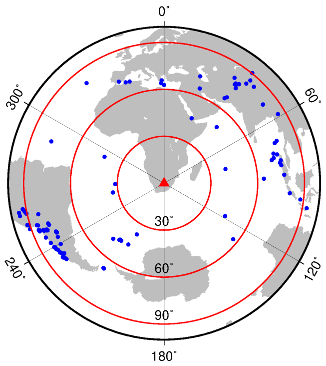

Figure 8. Location of station BOSA (red triangle) and distribution of selected events (blue dots).

0.04 and 0.08). For a velocity of 0, that is, without slowness correction, the energy of the Moho reflection is also very strong. Although this method also locates the local maximum of the Moho reflection energy cluster in this case, it is more difficult to locate this local maximum for the field data, due to the lower frequency and the presence of noise. Therefore, for the field data, we only use teleseismic phases with a horizontal slowness between 0.04 and 0.08.

Therefore, this velocity analysis method makes it possible to directly estimate the velocity distribution and subsurface structures. More importantly, it can be used to visualize the superposition process, which can help us distinguish between signals from true reflections and signals from interference.

3 Field data test for station BOSA

In this section, we first reproduce the work of Phạm and Tkali (2017) to demonstrate the validity of the velocity analysis method. BOSA is a permanent station on the Kaapvaal craton, South Africa. The Moho discontinuity is sharp and flat in a broad area beneath the craton (James, 2003), which is useful for recovering reflections using teleseismic P wave coda autocorrelation. The Moho discontinuity lies about 35 km below station BOSA, and both P and S wave velocities and density gradually increase with the depth in the crust. The average crustal P wave velocity is 6.37 km/s, so a conspicuous reflection from the Moho discontinuity will be recovered at about 11 s in the stacked autocorrelogram. These parameters allow us to perform a simple check of the validity of our method.

We selected events with a magnitude greater than 5.5 in the GCMT catalog and an epicentral distance ranging from 30 to 95 degrees from 2010 to 2015. The window length is 80 s, starting at 20 s before the P onset. The raw records were first processed to the remove the mean and trend, and then band filtered to [0.1 2] Hz using a 4-point Butterworth filter. Then 117 events with clear a P-wave onset and a high signal-to-noise ratio were visually selected. The location of station BOSA and selected events are shown in Figure 8. Due to the difference in individual selection criteria, we chose more events than Phạm and Tkali (2017) (about 80). This does not produce a significant difference in the stacked results, because the stacking step has good noise immunity.

Next, the frequency spectra of selected events were whitened in a similar manner to Phạm and Tkali (2017). However, we used a Gaussian smoothing method to obtain the smoothed amplitude spectrum rather than a running absolute mean. These methods are equivalent in terms of spectral whitening. The Gaussian window width controls

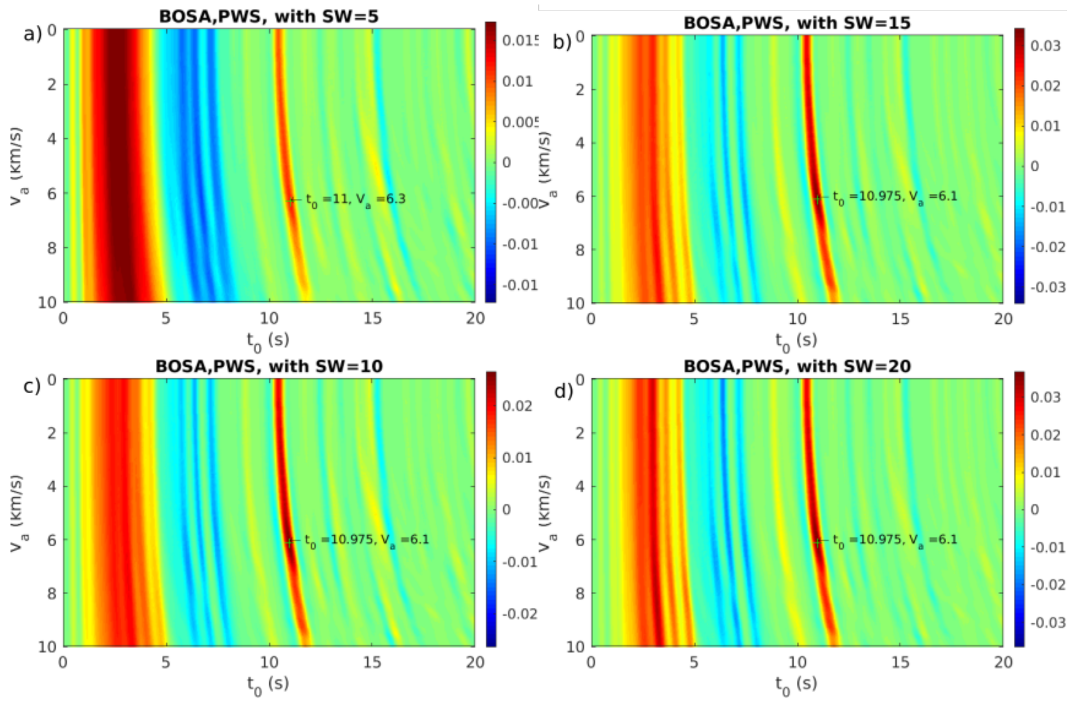

Figure 9. Velocity results for station BOSA with different smoothing window widths, of 5, 10, 15, and 20 points.

the global amplitude information retained in the whitened spectrum. The autocorrelograms of the whitened records are calculated and the causal parts were chosen as the recovered reflections after inverting the polarity. The velocity analysis results of the recovered reflections were calculated using Equation 13. The results of the velocity analysis with different smoothing window widths are shown in Figure 9. All subfigures contain an energy cluster at about 11 s, which. corresponds to the reflection from the Moho discontinuity below the station. This peak in the energy cluster is marked by a green cross, with the estimated average velocity and two-way travel time shown at the right. For a smoothing window width of 5 points, the estimated average velocity (6.3 km/s) is very close to the known velocity (6.37 km/s). However, strong artifacts are present before 10 s, which are related to the source time function. The other subfigures display the same estimated average velocity (6.1 km/s), which does not differ significantly from the known velocity. For a smoothing window width of 15 points, the energy cluster is more focused and the result contains fewer artifacts before 10 s than in the others. Hence, we consider a smoothing of 15 points to be optimal for spectral whitening. The recovered reflections for this case after moveout correction are shown in Figure 10. Coherent waveform are present at about 11 s.

In order to verify the stability of this method, we implemented 10,000 velocity analysis tests. In each test, 80% of the seismic records (94) were randomly selected from all 117 seismic records. The average velocity and vertical two-way travel time estimated from each test is shown in Figure 11. The distribution of the estimated average velocity and two-way travel time are more concentrated, indicating that the method proposed in this paper has good stability. Their medians are 6.1 km/s and 10.975 s, respectively. The calculated depth of the Moho discontinuity is 33.5 km. However, the estimated average velocity still has some serious deviations, which are not shown in the figure due to the very few occurrences. These deviations represent the influence of the data selection on the results. Figure 12 shows the results of the velocity analysis for the most deviated data

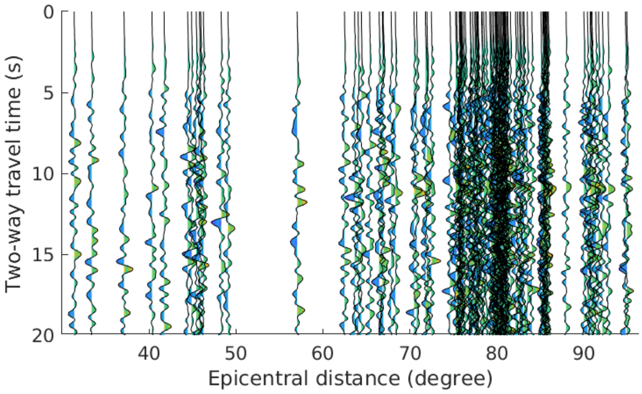

Figure 10. Reflections below station BOSA after moveout correction with the estimated average velocity (6.1 km/s).

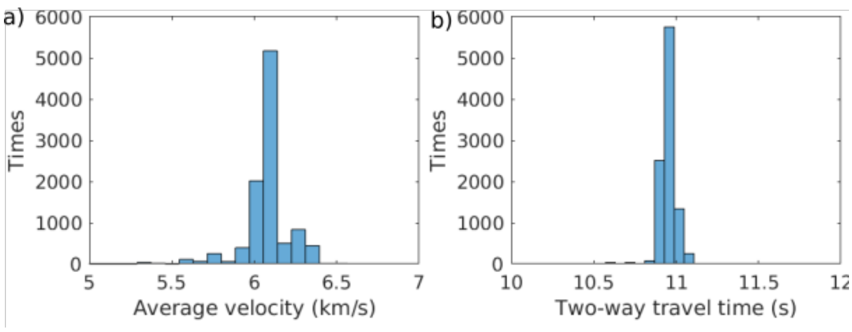

Figure 11. Distribution of estimated average velocity and vertical two-way travel time.

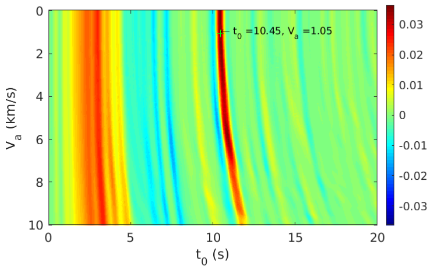

Figure 12. Velocity analysis result for the most deviated data set.

Figure 13. Location of the NCISP-6 seismic array. Red triangles represent 60 temporary stations in this dense array. Blue lines represent faults in this area (Deng et al., 2003).

set. In this case, the energy cluster at about 11 s is unfocused, which serves as a guide to the user to re-select the data.

Next, we will detail the processing workflow of our method as applied to the BOSA station. This method allows us to evaluate the reliability of the recovered reflection based on whether the energy cluster corresponding to the reflection is focused. This in turn guides us to select appropriate data and adjust the processing parameters. In addition, the estimated average velocity and two-way travel time allows us to directly estimate the depth of the Moho discontinuity when we do not fully understand the crustal velocity distribution. The above illustrates the successful application of our method in the case of sharp and flat Moho discontinuities. In the next section, we will examine the validity of this method in relatively complex situations.

4 Field data test for the NCISP-6 dense array

To verify the effectiveness of our method in relatively complex situations, we chose a dense array (NCISP-6) in Northeast China. The array was deployed by the Institute of Geology and Geophysics, Chinese Academy of Sciences, under the North China Interior Structure Project (NCISP). The location of the NCISP-6 seismic array and the faults in this area are shown in Figure 13.

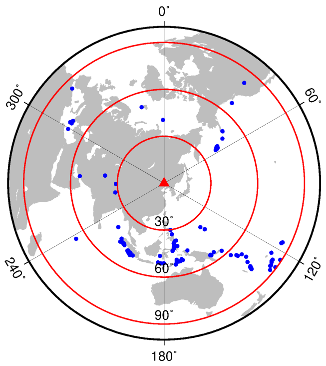

Figure 14. Distribution of selected events for station NE33

The stations are regularly distributed along a straight line, which facilitates our subsequent imaging. Zheng et al. (2015) presented a seismic image across the North China Craton (NCC) and Central Asian Orogenic Belt (CAOB) using a velocity structure imaging technique for receiver functions from the dense array. They showed that the Moho discontinuity in the NCC is about 34 km and deepens slowly to 40 km in the CAOB. The crust-mantle transition zone is relatively sharp in most areas of NCC and CAOB, except for the thick transition zone in the Tanlu fault. These features are convenient for testing the application of our method in regions of gradual incline and thicker transition regions of the Moho discontinuity.

4.1 Data selection and processing

We first take NE33 station as an example to illustrate the data processing workflow. First, we downloaded the events with epicentral distances between 30 and 95 degrees and a magnitude greater than 5.5 in the IRIS data management center using JWEED. The records have a time length of 80 s, starting at 20 s before the P onset. The mean and trend are then removed from the raw data. In order to facilitate data selection, the frequency of the preprocessed data is first filtered to between 0.1 and 2.0 Hz using a 4-point Butterworth bandpass filter. The phases are visually selected to include those with a clear P onset and high SNR, for a final total of 127 phases. Figure 14 shows the distribution of selected events.

In the next step, the spectra of selected data is whitened and then autocorrelated. The spectral whitening method used here is similar to the method of Phạm and Tkali (2017). The records are first converted to the frequency domain, then we use Gaussian smoothing to obtain a smoothed amplitude spectrum with a Gaussian smoothing window width of 20 points. The whitened amplitude spectrum is equal to the ratio of the original amplitude spectrum and the smoothed amplitude spectrum. Then we convert the whitened amplitude spectrum and phase spectrum to the time domain and filter it to [0.1-1.0] Hz using a 4-point Butterworth bandpass filter. The causal part of the autocorrelograms is then taken as the extracted virtual reflection responses, the result of which is shown in Figure 15. It is evident that the frequency spectrum of the autocorrelogram of different events is principally the same in this case and that overall, there is a clear Moho reflection at the 10 s position.

We then use Equation 13 to obtain the velocity analysis results (as shown in Figure 16). An obvious Moho reflection energy cluster can be seen between 10 s and 12 s, and the energy cluster is distributed along the reference velocity curve (blue curve). The reference velocity model (Figure 17) was extracted from the study of Xin et al. (2019). According to the location of the local maximum of the Moho reflected energy cluster,

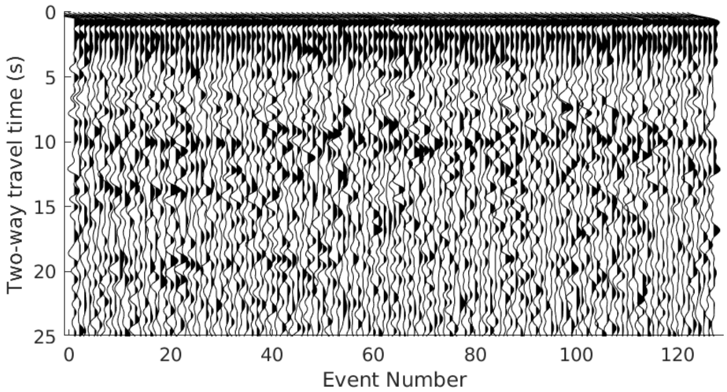

Figure 15. Autocorrelograms of station NE33 with spectral whitening.

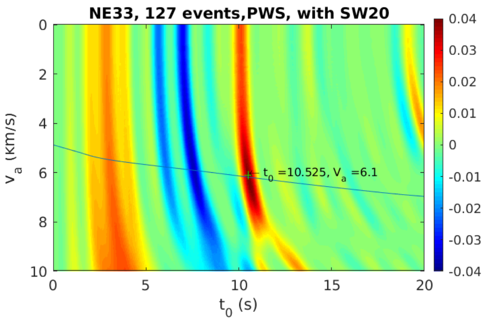

Figure 16. Velocity analysis result for station NE33. The records before 10 s are tapered by a Hanning window.

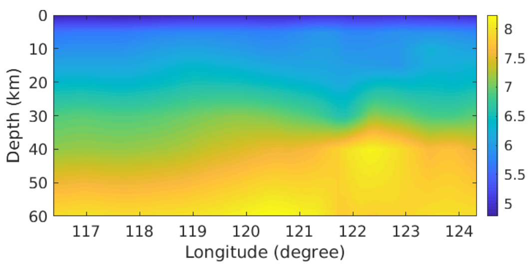

Figure 17. P-wave velocity below NCISP-6

Table 1. Velocity analysis summary

Station	F/N	Es	SW	Station	F/N	Es	SW	Station	F/N	Es	SW
$NE00$	F	50	40	$NE21$	F	56	50	$NE41$	F	83	30
$NE01$	N	55	–	$NE22$	F	79	50	$NE42$	F	71	20
$NE02$	F	38	10	$NE23$	N	52	–	$NE43$	F	92	10
$NE03$	F	52	30	$NE24$	F	86	70	$NE44$	F	103	10
$NE04$	F	43	60	$NE25$	F	82	70	$NE45$	F	62	10
$NE05$	F	52	50	$NE26$	N	75	–	$NE46$	F	58	30
$NE06$	F	43	10	$NE27$	N	84	–	$NE47$	F	92	10
$NE07$	F	65	40	$NE28$	N	89	–	$NE48$	F	56	10
$NE08$	F	61	10	$NE29$	F	51	70	$NE49$	F	79	10
$NE09$	F	82	20	$NE30$	F	68	40	$NE50$	N	73	–
$NE10$	F	66	30	$NE31$	F	71	40	$NE51$	N	51	–
$NE11$	N	74	–	$NE32$	F	69	20	$NE52$	F	65	20
$NE12$	F	72	10	$NE33$	F	127	20	$NE53$	F	75	30
$NE14$	F	53	10	$NE34$	N	54	–	$NE54$	F	69	40
$NE15$	F	54	40	$NE35$	F	57	50	$NE55$	F	75	50
$NE16$	F	45	40	$NE36$	F	67	20	$NE56$	F	78	10
$NE17$	F	41	20	$NE37$	F	74	10	$NE57$	N	52	–
$NE18$	F	45	20	$NE38$	F	75	50	$NE58$	F	86	20
$NE19$	N	21	–	$NE39$	N	101	–	$NE59$	F	74	10
$NE20$	F	60	20	$NE40$	F	83	50	$NE60$	F	57	20

[a]F/N denotes whether the energy cluster is focused or not.
[b]Es denotes the number of events selected.
[c]SW denotes the smoothing window width for spectral whitening.

we estimate that the average velocity of the crust is 6.1 km/s, which is consistent with the reference velocity. Based on this average velocity and the corresponding vertical two-way travel time (10.525 s) of the Moho reflection, we calculate the Moho depth below station NE33 to be approximately 32 kilometers. This is also in good agreement with the result of the receiver function (about 33 km, in Zheng et al. (2015)).

4.2 Results

We processed the data of the other 59 stations using the same procedure as at station NE33 (including spectral whitening and the PWS method). Due to space limitations, we summarize the velocity analysis results of all stations in Table 1. As shown in Table 1, obvious Moho-reflected energy clusters can be seen in the velocity analysis results of 48 stations (about 80%). This indicates good generalization of the velocity analysis method in the field data. Figure 18 presents several examples of these results. For the stations that have clear Moho reflection energy groups, such as stations NE9, NE21, NE41, and NE56, we consider their stacked reflections to be reliable. These velocity analysis results therefore provide an important reference that allows us to explain the stacked reflections.

The extracted reflections of 60 stations were stacked using Equations 9 and 11 where the first 10 seconds of each record was tapered. The reflections of the stations without clear Moho reflection energy group in the velocity analysis result were removed and linearly interpolated by neighboring stations. The interpolated results are shown in Figure 19. A clear and continuous Moho reflection can be seen at a position of more than 10 seconds in the figure. Next, we used an average velocity of 5 km/s to correct the station elevation to 0 meters. The reflection records were then converted to the depth do-

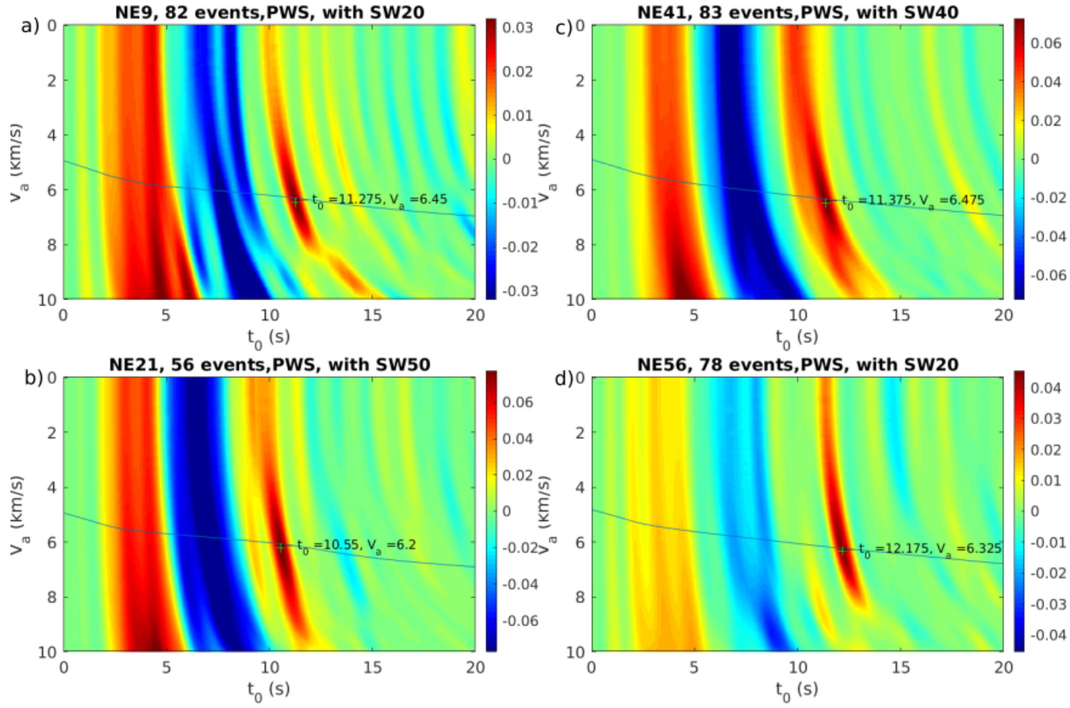

Figure 18. Examples of velocity results containing a clear energy group for the reflection from the Moho discontinuity.

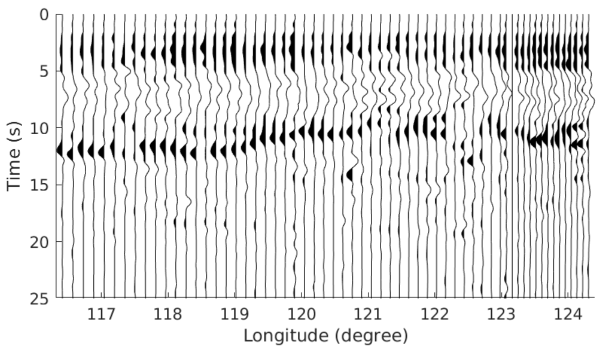

Figure 19. The recovered reflections from the Moho discontinuity below the NCISP-6 dense array.

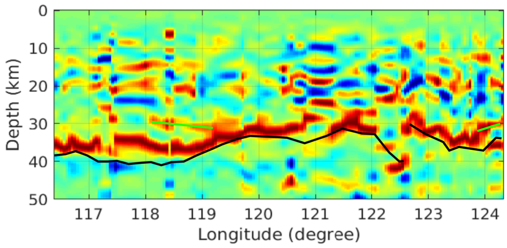

Figure 20. P-wave reflection image of crust-mantle structures below the NCISP-6 dense array. Black lines represent the Moho resolved by a receiver function. The lines were drawn by reference to Figure 3b in Zheng et al. (2015). Green lines represent a discontinuity in the lower crust.

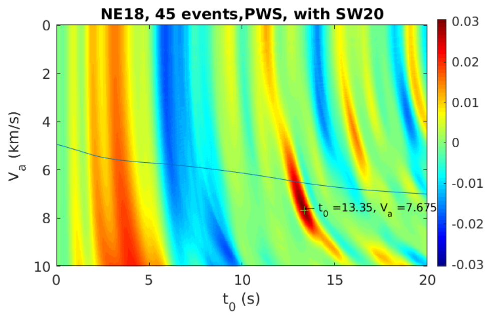

Figure 21. Velocity results of station NE18 at Tanlu fault

main according to the reference velocity model (Figure 17). The final imaging result is shown in Figure 20.

The position and shape of the Moho reflection in Figure 20 is very similar to the result of the receiver function (Figure 2a in Zheng et al. (2015)), but our result displays more detail. Specifically, in most areas of the NCC (longitude range of 119.5 to 123 degrees), the depth of the Moho is about 32 kilometers. The Moho deepens to about 38 kilometers in the transition zone between the NCC and the E-CAOB (longitude range of 118.5 to 119.5 degrees). On the east side of the NCC (longitude greater than 123 degrees), the Moho also deepens to about 35 kilometers. These characteristics are also consistent with the distribution of faults in Figure 13. At the Tanlu fault (longitude near 122.5 degrees), the depth of the Moho is about 40 kilometers, whereas for example, the Moho below station NE18 is at a depth of about 43 kilometers. The velocity analysis results show this feature. (Figure 21). These features are consistent with the interpretation of the receiver function (black lines in Figure 20).

5 Conclusions

We proposed a new velocity analysis method based on the horizontal slowness arrival formula. In the velocity analysis results, reliable reflections correspond to focused energy clusters along the reference velocity. Therefore, this method may become a standard for testing the reliability of reflections extracted by autocorrelation. Similarly to the $h-\kappa$ stacking method (Zhu & Kanamori, 2000) in the receiver function study, the velocity analysis result provides an average velocity above the interface and the vertical two-way travel time of the reflected wave, then calculates the depth of the interface.

The synthetic data tests indicate the reliability of this method. Through velocity analysis, we can determine which stacked reflections are reliable and which are not. Based on the average velocity distribution and the vertical two-way travel time provided by the velocity analysis results, we can even construct a relatively reliable velocity model. The field data test for bedrock station BOSA illustrates the successful application of the method in the case of a sharp and flat Moho discontinuity.

We also applied this method to the field data of the NCISP-6 dense array. Focused energy clusters of the Moho reflection can be clearly seen in the velocity analysis results of more than 80% of the stations. This demonstrates the applicability of this method to field data and through these focused energy clusters, we can evaluate the reliability of the extracted reflections. In the final image, the depth and shape of the Moho discontinuity are consistent with the result of the receiver function method. This validates the robustness of this method in relatively complex situations.

Not only can the velocity analysis results be used for final interpretation, but, it also aids in selecting appropriate parameters (data selection, filter frequency band, and spectrum whitening parameters, etc.) in the data processing step. Data selection and velocity analysis results can be easily realized by machine learning, which will help the method find applications to large-scale data in the future.

Obtaining a reliable reflected wave is the basis of using reflected waves to invert the velocity structure. With this foundation, we can use Bayesian inversion and other methods to invert the velocity structure. It can also be combined with the receiver function, the surface wave dispersion curve, gravity, and electromagnetic data. Finally, this method may be extended to the autocorrelation results of the radial component to obtain reliable S-wave reflections.

Acknowledgments

This work is supported by the China Postdoctoral Science Foundation (No. 2019M662172) and the National Natural Science Foundation of China (under grant no. 42074056). We also thanks the support of Shenzhen Science and Technology Program (Grant No. KQTD20170810111725321).

References

Claerbout, J. F. (1968). SYNTHESIS OF A LAYERED MEDIUM FROM ITS ACOUSTIC TRANSMISSION RESPONSE. *GEOPHYSICS*, *33*(2), 264–269. doi: 10.1190/1.1439927

Deng, Q. D., Zhang, P. Z., Ran, Y. K., Yang, X. P., Wei, M., & Chen, L. C. (2003). Active tectonics and earthquake activities in china. *Earth Science Frontiers*, *10*(S1), 66–73.

Gorbatov, A., Saygin, E., & Kennett, B. L. N. (2013). Crustal properties from seismic station autocorrelograms. , *192*(2), 861–870. doi: 10.1093/gji/ggs064

James, D. (2003). Crustal structure of the kaapvaal craton and its significance for early crustal evolution. , *71*(2), 413–429. doi: 10.1016/j.lithos.2003.07.009

Kennett, B. L. N. (1983). *Seismic wave propagation in stratified media.* London: Cambridge Univ. Press.

Nishitsuji, Y., Ruigrok, E., Gomez, M., Wapenaar, K., & Draganov, D. (2016). Reflection imaging of aseismic zones of the Nazca slab by global-phase seismic interferometry. *Interpretation*, *4*(3), SJ1–SJ16. doi: 10.1190/INT-2015-0225.1

Phạm, T.-S., & Tkali, H. (2017). On the feasibility and use of teleseismic P wave coda autocorrelation for mapping shallow seismic discontinuities: P Wave Coda Autocorrelation. *Journal of Geophysical Research: Solid Earth*, *122*(5), 3776–3791. doi: 10.1002/2017JB013975

Phạm, T.-S., & Tkali, H. (2018). Antarctic Ice Properties Revealed From Teleseismic P Wave Coda Autocorrelation. *Journal of Geophysical Research: Solid Earth*, *123*(9), 7896–7912. doi: 10.1029/2018JB016115

Plescia, S. M., Sheehan, A. F., Haines, S. S., Worthington, L. L., Cook, S., & Ball, J. S. (2020). Teleseismic p-wave coda autocorrelation imaging of crustal and basin structure, bighorn mountains region, wyoming, u.s.a. , 1–10.

Randall, G. E. (1994). Efficient calculation of complete differential seismograms for laterally homogeneous earth models. *Geophysical Journal International*, *118*(1), 245-254. doi: 10.1111/j.1365-246X.1994.tb04687.x

Ruigrok, E., & Wapenaar, K. (2012). Global-phase seismic interferometry unveils P-wave reflectivity below the Himalayas and Tibet: GLOBAL-PHASE SEISMIC INTERFEROMETRY. *Geophysical Research Letters*, *39*(11), n/a–n/a. doi: 10.1029/2012GL051672

Schimmel, M., & Paulssen, H. (1997). Noise reduction and detection of weak, coherent signals through phase-weighted stacks. *Geophysical Journal International*, *130*(2), 497-505. doi: 10.1111/j.1365-246X.1997.tb05664.x

Sun, W., Fu, L., Wei, W., & Tang, Q. (2018). A new seismic daylight imaging method for determining the structure of lithospheric discontinuity. doi: 10.1007/s11430-018-9249-3

Sun, W., & Kennett, B. L. N. (2016). Receiver structure from teleseisms: Autocorrelation and cross correlation: SEISMIC DAYLIGHT IMAGING. *Geophysical Research Letters*, *43*(12), 6234–6242. doi: 10.1002/2016GL069564

Sun, W., & Kennett, B. L. N. (2017). Midlithosphere discontinuities beneath the western and central North China Craton. *Geophysical Research Letters*, *44*(3), 1302–1310. doi: 10.1002/2016GL071840

Tork Qashqai, M., Saygin, E., & Kennett, B. L. N. (2019). Crustal imaging with bayesian inversion of teleseismic P wave coda autocorrelation. , *124*(6), 5888–5906. doi: 10.1029/2018JB017055

Xin, H., Zhang, H., Kang, M., He, R., Gao, L., & Gao, J. (2019). HighResolution Lithospheric Velocity Structure of Continental China by DoubleDifference Seismic TravelTime Tomography. *Seismological Research Letters*, *90*(1), 229–241. doi: 10.1785/0220180209

Zheng, T.-Y., He, Y.-M., Yang, J.-H., & Zhao, L. (2015). Seismological constraints on the crustal structures generated by continental rejuvenation in northeastern China. *Scientific Reports*, *5*(1), 14995. doi: 10.1038/srep14995

Zhu, L., & Kanamori, H. (2000). Moho depth variation in southern California from teleseismic receiver functions. *Journal of Geophysical Research: Solid Earth*, *105*(B2), 2969–2980. doi: 10.1029/1999JB900322